Heliyon 5 (2019) e01714

Contents lists available at ScienceDirect

Heliyon

journal homepage: www.heliyon.com

The synthesis of CB[8]/ZnO composites materials with enhanced photocatalytic activities

Lan Li, Lin Liu, Zhuang Li, Danling Hu, Chao Gao *, Jinyan Xiong **, Wei Li ***

Hubei Key Laboratory of Biomass Fiber and Eco-dyeing &F inishing, College of Chemistry and Chemical Engineering, Wuhan Textile University, Wuhan 430073, China

ARTICLE INFO

Keyword:
Materials chemistry

ABSTRACT

Enhancing the separation of hole-electron pairs is one of the valid pathway to enhance the photocatalytic degradation performance of semiconductors. In this work, cucurbit[8]uril/zinc oxide (CB[8]/ZnO) composites were prepared. The structure, morphology, surface elements and optical properties of the composite are characterized by powder X-ray diffraction, scanning electron microscopy, Fourier transform infrared spectroscopy, X-ray photoemission spectroscopy, thermogravimetric analysis, and specific surface area measurements. In the photocatalytic degradation of 500 mg/L reactive brilliant red X-3B and 400 mg/L reactive yellow X-RG solutions, the rate constant of the CB[8]/ZnO composite is six times that of pure ZnO. A possible photocatalytic degradation mechanism is proposed. Zn^{2+} ions chelate with the carbonyl group of CB[8] on the surface of CB[8]/ZnO. Under ultraviolet-visible light irradiation, the generated holes of ZnO are transferred to and trapped on the CB[8] units to facilitate the separation of electron-hole pairs, improving the photocatalytic performance of this system.

1. Introduction

Dyes are commonly used in the textile, food, pharmaceutical, leather, cosmetics, and paper industry. It is very necessary to remove dyes from effluent before its release into the natural environment, due to their low biodegradability and because they prejudicial to photosynthetic activities and toxic to aquatic organisms [1]. Various methodologies have been applied to remove dyes from industrial wastewater, including flocculation, flotation, biological processes, oxidation procedures, electrocoagulation, Fenton catalysis, membrane separation, and adsorption [2, 3, 4, 5, 6]. Among them, photocatalysis has attracted great interest as the most promising way to solve the environmental problems, especially by eliminating residual dye pollutants from the wastewater stream [7]. Several types of promising photocatalysts, including titanium dioxide (TiO_2) [8, 9], zinc oxide (ZnO) [10, 11, 12, 13], cuprous oxide (Cu_2O) [14, 15], and bismuth oxyhalides (BiOX) [16], have been actively applied in dye effluent remediation. A suitable band gap, ease of fabrication, low cost, and nontoxicity enable ZnO to be used extensively in photocatalysis [10, 11, 12, 13]. The fast recombination of holes and electrons, however, and low efficiency in the visible region due to its wide band gap limits its application. To improve the photocatalytic efficiency of ZnO in the visible region, ZnO based binary or ternary composites were developed by doping with graphene oxide (GO) [16], multi-walled carbon nanotubes (MWCNTs) [17], g-C_3N_4 [18], where g stands for graphitic, and metals [19]. Furthermore, biopolymers [20], cellulose [21], and oligoaniline [22] were coupled with ZnO to enhance the adsorption capacity of ZnO, and the synergistic effects of adsorption and photocatalysis towards the removal of dyes were investigated.

Cucurbit[n]urils (CB[n]s) with rigid structure and a hydrophobic interior can efficiently adsorb organic dyes [23], especially CB[8], which presents super-high capacity towards the removal of reactive and acidic dyes due to the suitable size of its cavity [24, 25, 26]. Cucurbit[n]urils (CB[n]) have also been used as trapping agents for holes or electrons to facilitate hole-electron separation [27, 28, 29, 30]. For example, in polyoxometalate-cucurbituril molecular solids, metal ions chelate with carbonyl groups of the cucurbiturils; the charge transfer between polyoxometalate and cucurbituril enhances the separation of hole–electron pairs to improve photocatalytic efficiency [27, 28, 29]. In the CdS/CB[5] composites, the generated holes of CdS were attracted by the electron-rich carbonyl groups of CB[5], and the separation of electron-hole paitd significantly enhanced the photocatalytic efficiency of this system [30].

* Corresponding author.
** Corresponding author.
*** Corresponding author.
E-mail addresses: chgao@wtu.edu.cn (C. Gao), xjybear@163.com (J. Xiong), liwei_whu@sohu.com (W. Li).

https://doi.org/10.1016/j.heliyon.2019.e01714
Received 11 February 2019; Received in revised form 28 April 2019; Accepted 9 May 2019

In this work, cucurbit [8]uril (CB[8]) was selected as a hole or electron trapping agent to couple with ZnO. The prepared composites were characterized, and the photocatalytic activity was tested on the degradation of reactive dyes under ultraviolet (UV)-visible light. The photocatalytic degradation mechanism was explored.

2. Experimental

2.1. Materials

CB[8] was synthesized and purified according to references [31, 32]. Zinc nitrate hexahydrate ($Zn(NO_3)_2$•$6H_2O$), Sodium hydroxide (NaOH), 1, 2-propylene glycol, and ethanol were purchased from Sinopharm Chemical Reagent Co., Ltd (China) and were of analytical pure grade. Reactive yellow X-RG (with a dye content of 99%) and reactive brilliant red X-3B were commercial grade and were purchased from Shanghai Jiayin Chemical Engineering Co., Ltd (China). All reagents were used without any additional purification.

2.2. Preparation of CB[8]/ZnO composite

A schematic illustration of the synthetic procedure for CB[8]/ZnO composite was presented in Scheme 1. 0.159 g CB[8] (0.12 mmol) was dispersed in a mixed solution composed of 9.5 mL H_2O and 30 mL 1,2-propanediol under magnetic stirring, then 0.25 mL of 2.4 mol/L $Zn(NO_3)_2$ solution was added, and finally, 0.25 mL of 9.6 mol/L NaOH solution was added to the above solution dropwise, and the reaction was continued for 2 h. A mass of white precipitate was produced. After centrifugation, the obtained solid was washed repeatedly with deionized water and ethanol, and dried at 120 °C.

2.3. Materials characterization

The crystal structure of the CB[8]/ZnO composite was determined by powder X-ray diffraction (PXRD). XRD patterns were recorded on an Ultima IV diffractometer (Rigaku, Japan) (CuKα radiation, $\lambda = 1.54182$ Å). XRD data were collected in the 2θ range from 10° to 80° using step scan mode with step width of 0.02°. The FESEM images, EDX spectra and element mapping images were provided by a SU8010 scanning electron microscope (Hitachi, Japan) equipped with a energy dispersive spectroscopy. The Fourier transform infrared (FT-IR) spectra were recorded on a TENSOR-27 FT-IR spectrometer (Bruker, Germany) using the KBr wafer technique with a resolution of 4 cm^{-1} in the range of 400–2000 cm^{-1}. X-ray photoelectron spectra (XPS) were collected on an ESCALAB 250Xi X-ray photoelectron spectrometer (Thermo Fisher, USA). Thermogravimetric analysis (TGA) was performed on an 1100SF thermogravimetric analyzer (Mettler, Switzerland), on which a 10 mg sample were heated in an alumina pan with a 10 °C/min heating rate from 50 °C to 1000 °C under flowing N_2 (50 mL/min). The nitrogen adsorption-desorption analysis was conducted using a Micromeritics TriStar II 3020 analyzer (Micromeritics, USA) at 77.4K. Each sample was degassed at 110 °C for 120 min prior to analysis. The specific surface areas were calculated by the Brunauer-Emmett-Teller (BET) method. Photocurrent measurements and electrochemical impedance spectroscopy (EIS) were carried using a CHI660E electrochemical workstation. The photoluminescence (PL) spectrum of CB[8]/ZnO composite was collected between the wavelengths of 220 nm and 700 nm under excitation by a Xenon lamp laser with a 321 nm line using an F-2500 fluorescence spectrophotometer (Hitachi, Japan) at room temperature.

2.4. Photocatalytic activity test

The photocatalytic activity of CB[8]/ZnO composite was evaluated by measuring the photocatalytic degradation of X-3B and X-RG dyes under UV-visible (vis) light irradiation. The amount of catalyst was 50 mg, the volume of treated solution was 50 mL, and the initial concentrations of the X-3B and X-RG reactive dyes were 100–500 mg/L and 200–1000 mg/L, respectively. Before irradiation with UV-visible light, the system was left in the dark for 120 min to reach adsorption-desorption equilibrium of the dye on the surface of the photocatalyst. 2 mL of the suspension was collected at every 5 min interval, the supernatant liquid was obtained by centrifugal separation, and the residual dye was examined. The degradation rate (D) was calculated with the following formula:

$$D = \frac{C_0 - C_e}{C_0} \times 100\% \quad (1)$$

where D is the degradation rate, and C_0 and C_e are the initial concentration and residual concentration of dye, respectively.

3. Results and discussion

3.1. Photocatalyst characterization

3.1.1. XRD analysis

Powder XRD analysis was carried out to investigate the crystal structure of CB[8]/ZnO composite (Fig. 1). In the XRD pattern of the as-prepared pure ZnO, the sharp and narrow diffraction peaks with 2θ values of 31.74°, 34.37°, 36.34°, 47.66°, 56.52°, 63.09°, 66.53°, 68.01°, and 69.15° were indexed as reflections of the (100), (002), (101), (102), (110), (103), (200), (112), and (201) hlk crystal planes. These peaks confirm the formation of a cubic phase structure of ZnO nanoparticles (NPs). These peaks are in agreement with JCPDS card No. 36-1451. There is no obvious diffraction peak for CB[8] except for some rambling peaks between 10° and 35°. The XRD pattern of CB[8]/ZnO composite presents all the peaks of ZnO and CB[8]. The peak hkl indices, such as (100), (002), (101), (102), (110), (103), (200), (112), and (201), indicate cubic ZnO phase, and the rambling peaks arise from the CB[8]. It was observed

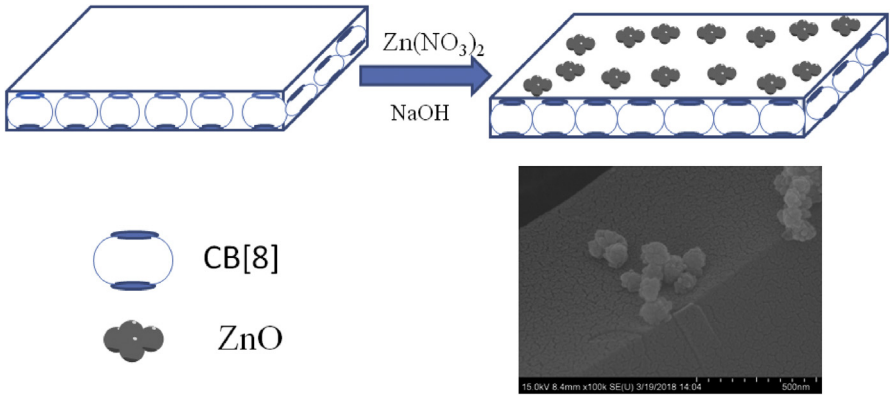

Scheme 1. Schematic illustration of the synthesis procedure for CB[8]/ZnO composite.

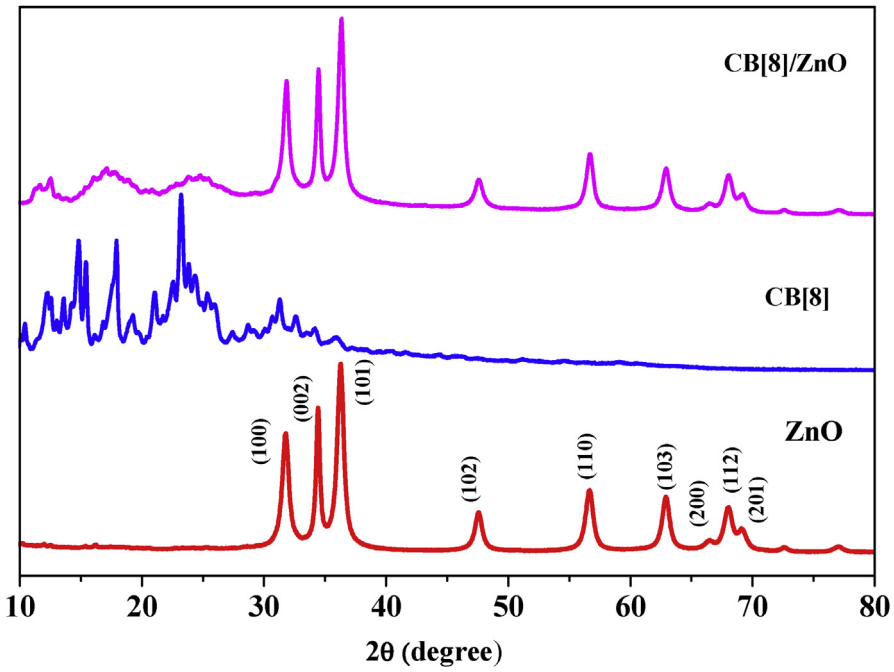

Fig. 1. XRD patterns of ZnO, CB[8], and CB[8]/ZnO nanocomposite.

that there were no extra diffraction peaks for other phases. The peak positions of ZnO were not shifted, suggesting that the CB[8] does not change the crystal type of ZnO.

3.1.2. SEM analysis

The micromorphology of the CB[8], ZnO, and CB[8]/ZnO composite was observed by scanning electron microscopy (SEM) and were presented in Fig. 2. The EDX elemental mapping analysis and EDX element composition analysis of CB[8]/ZnO composite were presented in Fig. 2 and Table 1, respectively. The morphology of ZnO can be observed in Fig. 2a. Pure ZnO is in the form of small globular aggregates, and the average size is about 20–40 nm. The overall morphology of CB[8] can be seen from Fig. 2b, where CB[8] exhibits irregular granular shapes with a size of 2–8 μm. The SEM micrograph of CB[8]/ZnO composite is presented in Fig. 2c. It is clear that ZnO nanoparticles were deposited on the surface of CB[8]. As shown in Fig. 2d, EDX mapping images confirm the good distribution of the four elements of C, O, N and Zn, which demonstrates that both the ZnO and CB[8] contribute to the formation of

Table 1
The EDX element composition analysis for CB[8]/ZnO composite.

Elements	Apparent concentration	K ratio	wt%	wt% Sigma
C	40.41	0.4041	56.04	0.50
N	15.54	0.0277	29.75	0.58
O	3.84	0.0129	13.22	0.28
Zn	0.79	0.0079	1.00	0.07
Total			100.00	

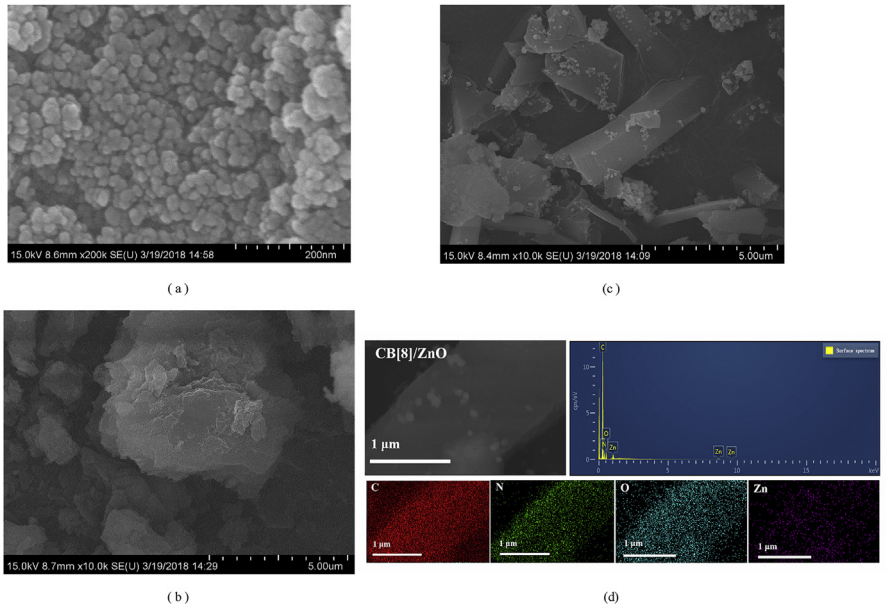

Fig. 2. SEM images of ZnO (a), CB[8] (b) and CB[8]/ZnO composite (c) and the elemental mapping analysis of CB[8]/ZnO composite(d).

the photocatalyst composites.

3.1.3. FT-IR spectral analysis

The FT-IR spectra of ZnO, CB[8], and CB[8]/ZnO composite are presented in Fig. 3. The main absorption bands were assigned according to references [24, 25, 26, 33] and presented in Table 2. On inspection of the IR spectrum of ZnO, it can be found that the band at 1633 cm^{-1} arises from the O-H bending vibration of water on the ZnO crystal surface, and the bands at 543 and 433 cm^{-1} arise from the Zn-O stretching vibration [33]. In the FT-IR spectrum of CB[8], the C=O stretching vibration of the carbonyl group appears at 1728 cm^{-1}, the bending and in-plane wagging vibration of methylene appears at 1474 and 1423 cm^{-1}, and the skeletal vibration of the glycoluril ring appears at 1375 cm^{-1}. The asymmetric stretching of N-C-N on the glycoluril ring appears at 1320 and 1230 cm^{-1}. The C-N stretching vibration can be observed at 970 cm^{-1}, the out-of-plane deformation vibration of the glycoluril ring can be observed at 807, 755, 674, and 631 cm^{-1}, and the tilting of cucurbituril ring appears at 445 cm^{-1} [24, 25, 26].

Comparing the IR spectrum of CB[8]/ZnO composite with those of CB [8] and ZnO, it is clear that CB[8]/ZnO composite possesses all the observable absorption bands of CB[8] and ZnO. The deposition of ZnO on the surface of CB[8] does not change the IR spectrum of CB[8], with the exception of ν(C=O), the bending and wagging vibration of methylene, and the skeletal vibration of the glycoluril ring. The ν(C=O) is shifted from 1728 cm^{-1} to 1722 cm^{-1}; the skeletal vibration of the glycoluril ring is shifted from 1375 cm^{-1} to 1382 cm^{-1}; and the bending and wagging vibrations of methylene are shifted from 1474 and 1423 cm^{-1} to 1476 and 1426 cm^{-1}, respectively; and the ν(Zn-O) is shifted from 553 cm^{-1} to 559 cm^{-1}.

To explain these IR shifts and explore the interaction of ZnO and CB [8], a 1:1 C[8]/ZnO simplified model was developed. On inspection of the single crystal structures of the polyoxometalate-cucurbituril molecular solid [27, 28, 29] and that of the supramolecular compound composing of cucurbit [8]uril and cobalt(III) complex [34], the metal cations were found to be chelated with the carbonyl groups of CB[n] to form a complex. Therefore, in the 1:1 CB[8]/ZnO model, the Zn^{2+} was designed to chelate with the carbonyl groups on the port of CB[8]. The ground state geometry was optimized by the density functional theory (DFT) method employing the B3LYP hybrid functional. The 6-31G(d) basis set was adopted for C, H, O, and N atoms and the LanL2DZ pseudo-potential basis set was applied for Zn atoms. A vibrational frequency calculation was carried out at the same level on the optimized geometry. All calculations were performed on the Gaussian09 revision D1 program suite [35]. The spectrum was simulated by the GaussSum 3.0 program [36] with a Lorentzian line shape, and the full width of half maximum (FWHM) of each peak was 15 cm^{-1}. The lack of any imaginary frequency reveals that the optimized geometry is on the local lowest point of the potential energy surface. The ground state geometry is presented in Fig. 4a. The calculated vibrational wavenumbers were compared with the experimental ones and are presented in Table 2. The simulated spectrum is presented in Fig. 4b. The DFT calculations could well reproduce the peak positions, and the deviations are within 20 cm^{-1}. The consistency between the simulated and experimental spectra

Table 2
The observed adsorption bands (cm^{-1}) of CB[8], ZnO, and CB[8]/ZnO composite, and the calculated IR bands of 1:1 CB[8]/ZnO complex.

Assignment[a]	Observed frequency (cm^{-1})			Calculated[b]
	CB [8]	ZnO	CB[8]/ZnO	1:1 CB[8]/ZnO
υ(C=O)	1728		1722	1727.7
σ(O-H)		1633	1634	1641.3
$\sigma(CH_2)$	1474		1476	1483.0
$\omega(CH_2)$	1423		1426	1424.4
skeletal vibration of glycoluril ring	1375		1382	1408.2
υ_{as}(N-C-N) of glycoluril ring	1320		1319	1323.7
υ_{as}(N-C-N) of glycoluril ring	1230		1232	1242.3
υ(C-N-C)	1187		1191	1187.3
υ(C-N)	970		971	971.3
Out-of-plane def of glycoluril ring	807		807	810.2
Out-of-plane def of glycoluril ring	755		753	765.0
Out-of-plane def of glycoluril ring	674		673	662.3
Out-of-plane def of glycoluril ring	631		631	630.1
Tilting of glycoluril ring	445		445	429.0
υ(Zn-O)		553	559	558.7
υ(Zn-O)		433		

[a] υ: stretching; σ: scissoring; ω: wagging; as: asymmetric; def: deformation.
[b] The calculated wavenumber of υ(C=O) mode were calibrated with scaling factor 0.93; the calculated wavenumber of υ_{as}(N-C-N), υ(C-N-C) and υ(C-N) mode were calibrated with scaling factor 0.98.

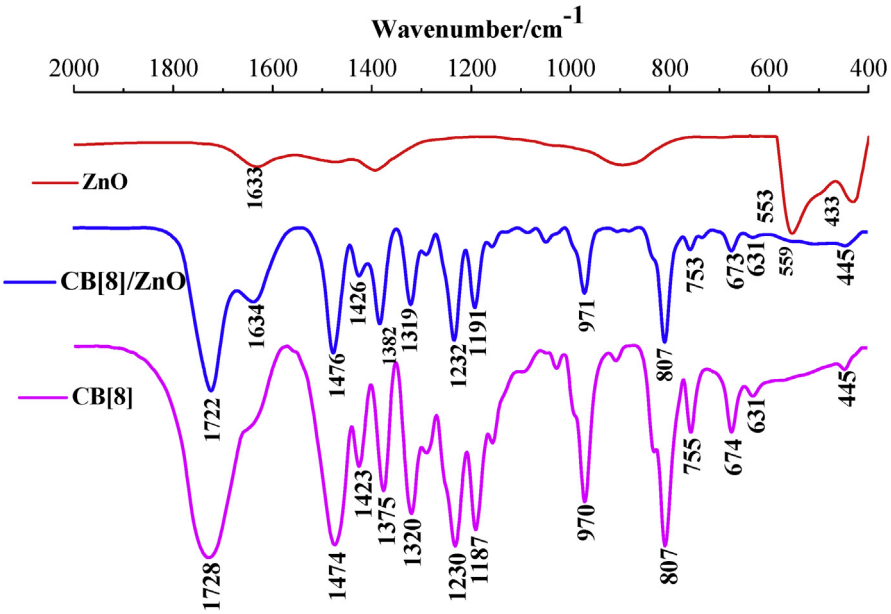

Fig. 3. The FT-IR spectra of CB[8], ZnO, and CB[8]/ZnO composite.

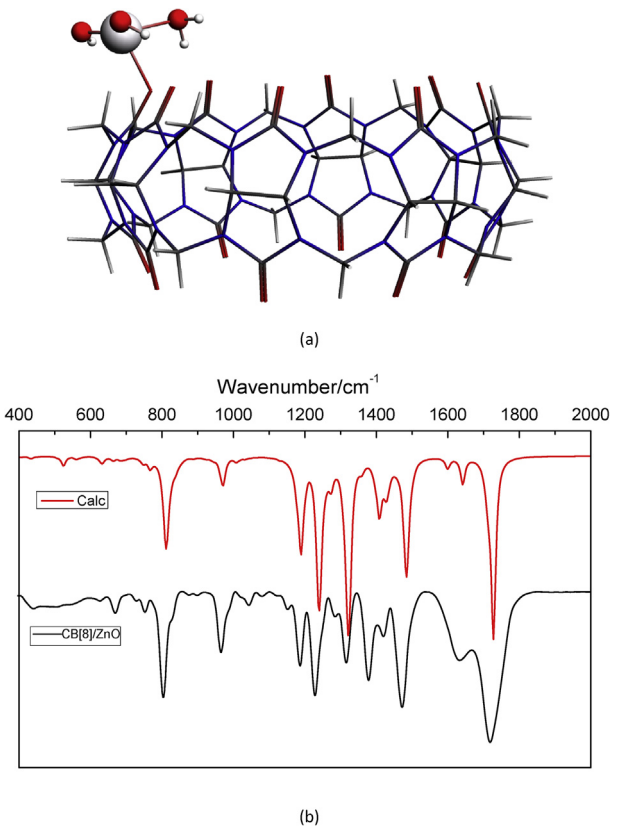

Fig. 4. The optimized ground state geometry of 1:1 CB[8]/ZnO on the B3LYP/Lanl2dz/6-31G(d) level of theory (a), and a comparison of the experimental and simulated IR spectra (b).

suggests that CB[8]/ZnO may exist in the form presented in Fig. 4a, where the Zn^{2+} is bonded with the hydroxy group and the carbonyl group of CB[8] to form a complex.

3.1.4. TG analysis

Thermogravimetric (TG) analysis was conducted on CB[8], CB[8]/ZnO composite, and ZnO, as shown in Fig. 5. CB[8] loses its coordinating water at 50–98 °C with a 13.0% weight loss. The decomposition of CB[8] starts at 394 °C and reaches a peak at 463 °C, and the weight loss ratio is 52.4%. Its charring takes place at 464–1000 °C with 19.9% mass loss [37]. Up to 1000 °C, zinc oxide only has a water loss process and is not broken down. CB[8]/ZnO composite loses its coordinating water at 95–100 °C with 5% weight loss. The first decomposition starts at 376 °C and reach a peak at 486 °C, and the weight loss ratio is 45.0%. This section corresponds to the decomposition stage of CB[8]. The second decomposition stage starts at 716 °C and reaches a peak at 791 °C, and the weight loss ratio is 19.2%. This section corresponds to the decomposition of the inclusion complex of CB[8] and $Zn(NO_3)_4]^{2-}$ or $[Zn(OH)_4]^{2-}$. The initiating decomposition temperature of the first stage was reduced from 394 °C to 376 °C, but the peak value was raised from 463 °C to 486 °C. The reduction of the decomposition temperature may have arisen from the loss of water encapsulated in the cavities of CB[8], and the elevation of the decomposition temperature may arise from the chelating of Zn^{2+} with the carbonyl groups on the port of CB[8] [34].

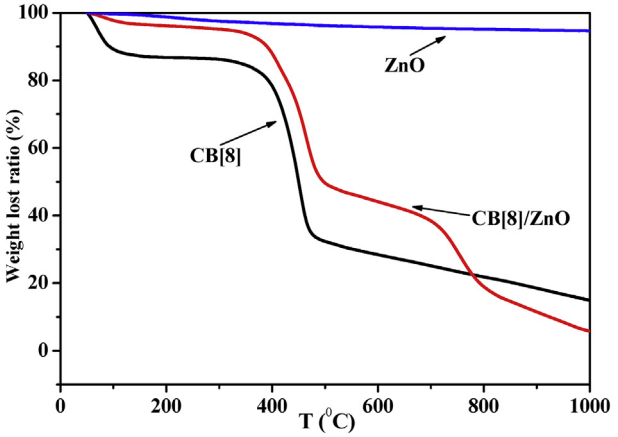

Fig. 5. TG curves of CB[8], ZnO, and CB[8]/ZnO composite.

3.1.5. XPS analysis

To further confirm the elemental compositions of the obtained samples, X-ray photoelectron spectra (XPS) of the prepared samples were obtained, as shown in Fig. 6. The full spectrum of XPS indicates that the composite is composed of Zn, O, C and N, and no other impurities are introduced into the composite process. XPS spectra of Zn 2p, C 1s, O 1s and N 1s were shown in Fig. 6b-e. The peaks located at 1021.58 eV and 1044.68 eV could be attributed to the characteristic binding energy of Zn 2p3/2 and Zn 2p1/2 [38]. There are three distinctive peaks of the C 1s core level of CB[8] at 284.82 eV, 287.20 eV, and 288.80 eV (Fig. 6c), which correspond to the C-C bonds, C-N bonds, and C=O bonds, respectively. The N 1s peaks at 399.91 eV corresponds to the amino groups of CB[8]. Fig. 6d presents the O 1s peak of the CB[8]/ZnO composite, and the peak at 531.78 eV corresponds to the lattice oxygen in the normal metal oxide crystal structure. Inspection of the XPS of Zn 2p in ZnO and CB[8]/ZnO composite, a significant shift toward higher energy section can be observed, which revealing the electrons are transferred from ZnO to CB[8].

3.1.6. BET analysis

N_2 adsorption and desorption experiments were carried out on the CB[8]/ZnO composite. The adsorption-desorption isotherms at 77.4 K are presented in Fig. 7, and the textural parameters are summarized in Table 3. A type H3-type hysteresis loop was observed in the adsorption-desorption isotherms of CB[8], ZnO and CB[8]/ZnO composite, suggesting the occurrence of capillary condensation and the existence of mesopores. As shown in Table 3, the pore volumes of CB[8] and ZnO are 0.020 cm^3/g and 0.079 cm^3/g, and the average pore diameters are 6.2 nm and 5.6 nm, respectively, indicating that all materials are mesoporous materials. The BET surface areas of CB[8] and ZnO were found to be 8.6 m^2/g and 55.4 m^2/g, respectively. SEM reveals that the ZnO nanoparticles were deposited on the surface of CB[8] in CB[8]/ZnO composite, and therefore, the textural parameters of CB[8]/ZnO composite were influenced by the addition of ZnO. In detail, the BET surface area, pore volume, and average pore diameter of CB[8]/ZnO are 13.0 m^2/g, 0.014 cm^3/g, and 4.7 nm, respectively.

3.1.7. Photoluminescence spectra

The photoluminescence (PL) spectrum provides useful information for the investigation of the charge carrier transfer at interfaces and the photogenerated electron-hole recombination process in the CB[8]/ZnO composite system. The PL spectra of ZnO and CB[8]/ZnO catalyst are presented in Fig. 8. In general, a reduced PL intensity indicates a low recombination rate of the photoinduced electrons and holes under light irradiation [14]. It can be found that the addition of CB[8] significantly reduces the fluorescence intensity of ZnO. This means that CB[8] can reduce the recombination rate of photoexcited electron-hole pairs from ZnO and facilitate the separation of the photoinduced electrons and holes.

3.1.8. Analysis of photoelectric properties of ZnO and CB[8]/ZnO composite

Such efficient charge separation of CB[8]/ZnO composite was experimentally supported by the transient photocurrent responses and electrochemical impedance spectra (EIS). Apparently, the photocurrent

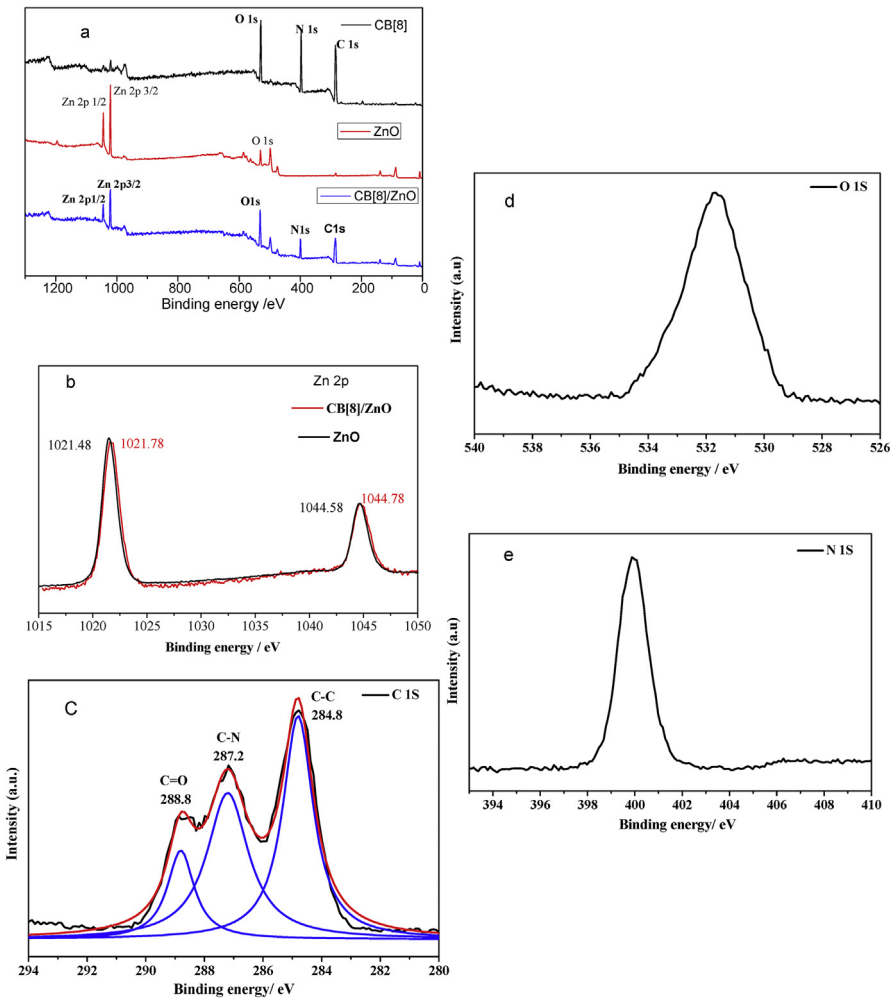

Fig. 6. The XPS spectra for ZnO, CB[8] and CB[8]/ZnO composite: (b) the Zn 2p, (c) C 1s, (d) O1s and (e) N 1s.

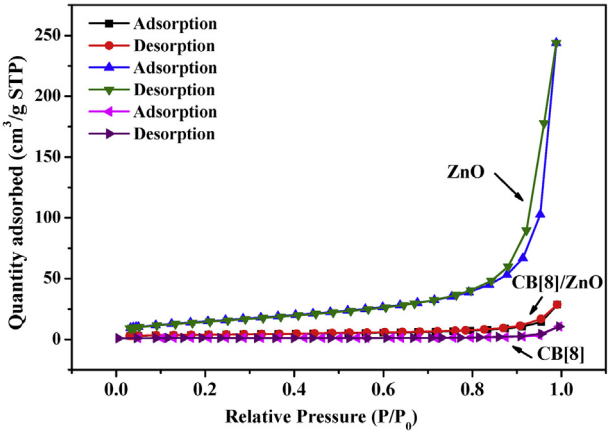

Fig. 7. N_2 adsorption-desorption isotherms for the samples at 77.4K.

density of pure ZnO is about six times that of CB[8]/ZnO composite as shown in Fig. 9a. However, according to EDX element composition analysis of CB[8]/ZnO composite (Table 1), the actual mass percent of ZnO is only 1.4%. For the same mass, the photocurrent density of ZnO in the composite is about twelve times that of pure ZnO. The EIS Nyquist plots (Fig. 9b) shows that CB[8]/ZnO composite has a smaller arc radius than pure ZnO. The smaller radius of the semicircular arc revealed a faster transfer of charge carriers in CB[8]/ZnO composite.

Table 3
Textural characteristics of CB[8], ZnO, and CB[8]/ZnO composite.

Adsorbents	BET surface area (m^2/g)	Pore volume (cm^3/g)	Average pore diameter (nm)
CB[8]	8.6	0.020	6.2
CB[8]/ ZnO	13.0	0.014	4.7
ZnO	55.4	0.079	5.6

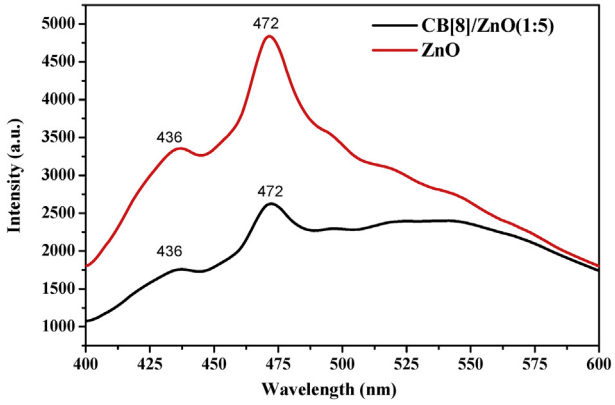

Fig. 8. Photoluminescence spectra of ZnO and CB[8]/ZnO composite.

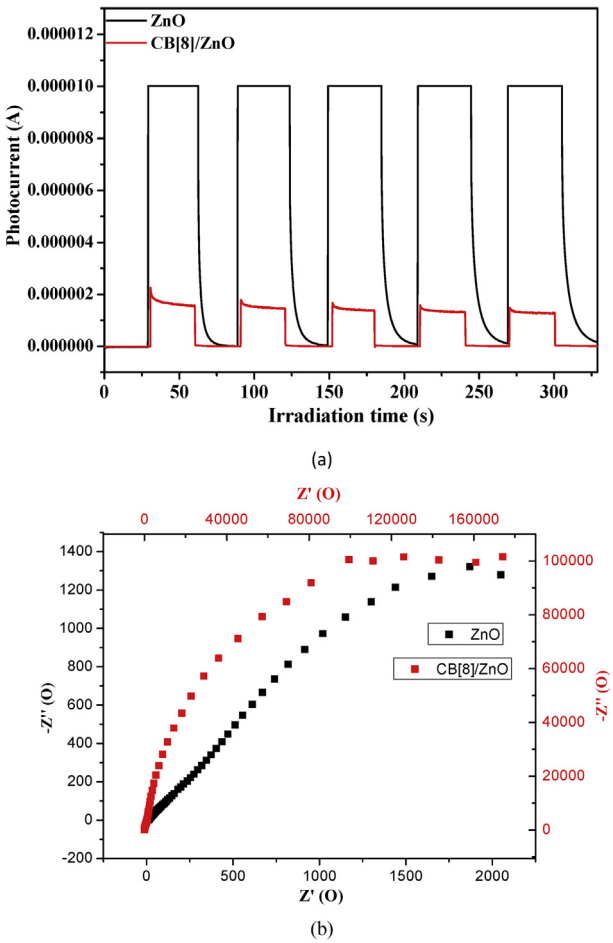

Fig. 9. The transient photocurrent responses (a) and Electrochemical impedance spectrum (b) of ZnO and CB[8]/ZnO composite.

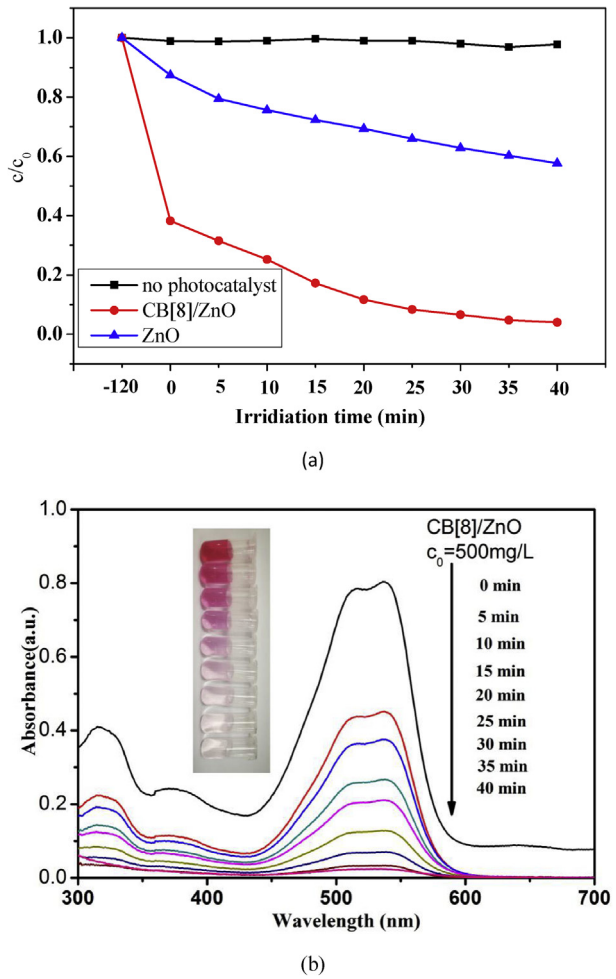

Fig. 10. Photocatalytic degradation of X-3B over pure ZnO and CB[8]/ZnO photocatalyst under UV-vis irradiation (c_0(X-3B):500 mg/L) (a) and the UV-vis absorption spectrum of X-3B under UV-vis irradiation after different time intervals using CB[8]/ZnO photocatalyst (b), with the inset showing a photograph of vials of the irradiated X-3B solution at the corresponding stages.

3.2. Photocatalytic activity

3.2.1. Photocatalytic degradation of reactive brilliant red X-3B dye

The photocatalytic activity of the as-obtained CB[8]/ZnO composite was evaluated by testing the degradation of X-3B solution at a concentration of 500 mg/L. Prior to irradiation, the photocatalytic reaction system was magnetically stirred in the dark for 120 min to reach the adsorption/desorption equilibrium of dye molecules on the surface of the photocatalyst. The photocatalytic performances of CB[8]/ZnO composite and pure ZnO nanoparticles are shown in Fig. 10. The photocatalytic degradation (PCD) results were fitted to pseudo-first-order kinetics, and the apparent rate constant k was calculated from $\ln(c/c_0) = kt$, where k represents the rate constant (min^{-1}), c_0 and c are the initial concentration of the dye and the residual concentration of the dye at time t, respectively.

The PCD efficiency for ZnO is 42.4%, with a rate constant of 0.0099 min^{-1}, after 40 min of UV–visible light irradiation. The PCD efficiency of CB[8]/ZnO composite is 95.9%, and the rate constant is 0.0610 min^{-1}, after 40 min of illumination. The corresponding UV-vis absorption spectrum of X-3B at different time intervals along with the color changes of the solution (inset) is presented in Fig. 10b. The 500 mg/L X-3B dye solution can be decolorized completely after 40 min irradiation. The PCD efficiency and rate constant of CB[8]/ZnO photocatalyst are twice and six times those of pure ZnO photocatalyst, respectively. CB[8] has superhigh adsorption capacity towards the adsorption of X-3B dye. Adsorption not only significantly improves the dye removal ratio in the dark reaction, but also significantly enhances the photocatalytic degradation rate in the light reaction. The SEM micrograph in Fig. 2c shows that the ZnO nanoparticles are distributed sporadically on the surface of CB[8], a great deal of unoccupied CB[8] surface ensures the adsorption of X-3B dye. XPS analysis has confirmed that there is electron transfer from ZnO to CB[8]. The charge transfer inhibits the recombination of photoelectrons and holes, and enhances the photocatalytic degradation efficiency [27, 28, 29]. Zhang reported 400 mg/L X-3B degradation under UV-vis/microwave irradiation and obtained a 100% removal ratio after 180 min of irradiation [38]. In comparison, CB[8]/ZnO photocatalyst yields a comparable PCD efficiency for a higher concentration (500 mg/L) within a shorter irradiation time (40 min).

3.2.2. Photocatalytic degradation of reactive yellow X-RG dye

In order to verify further the PCD efficiency of CB[8]/ZnO photocatalyst towards the removal of reactive dyes, an additional photocatalytic experiment was carried out on reactive yellow X-RG dye solution, and the results were presented in Fig. 11. The photocatalytic degradation rates were fitted with pseudo-first-order kinetics. It is clear that CB[8]/ZnO photocatalyst presents a very high performance towards the removal of X-RG dye. The PCD efficiency is 90.6%, and the rate constant k is 0.0603 min^{-1}, after 28 min of UV-vis light irradiation. The photocatalytic degradation rate decreased from 99% to 62.9% as the concentration of X-RG increased from 100 mg/L to 1000 mg/L. The high efficiency of CB[8]/ZnO towards the removal of reactive dyes in aqueous solution proves the existence of a synergetic effect between CB[8] and

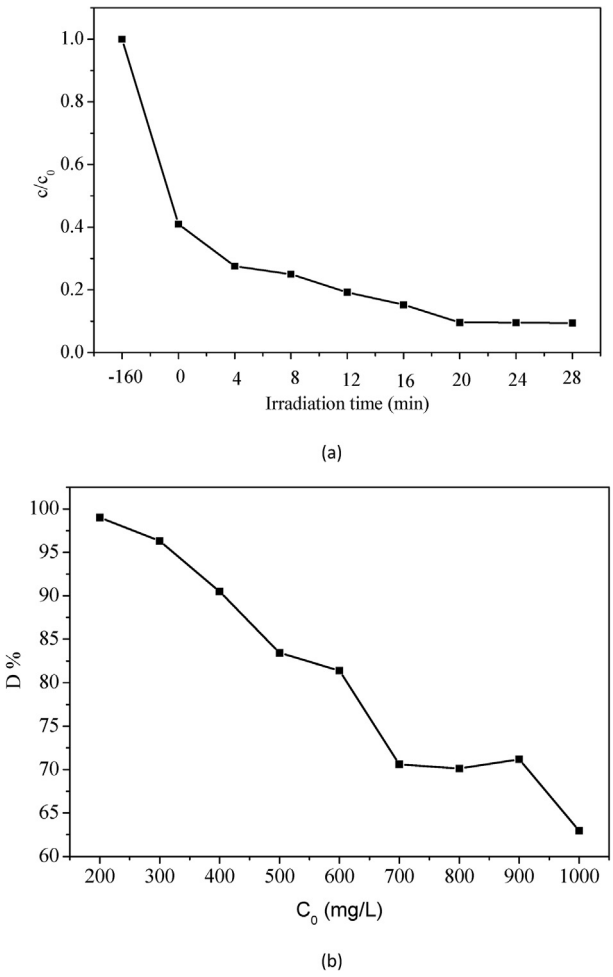

Fig. 11. Photocatalytic degradation of X-RG dye over CB[8]/ZnO composite (c_0(X-RG):400 mg/L) (a) and the degradation rate (*D*%) of X-RG dye solution for different concentrations (b) under UV-vis light irradiation.

the inorganic photocatalyst.

3.2.3. *Recyclability of CB[8]/ZnO photocatalyst*

With the purpose of evaluating the stability of CB[8]/ZnO photocatalyst, recycling experiments under UV-vis light irradiation were performed for five cycles with the same dye. The experimental conditions and the photocatalytic degradation rate (*D*%) are listed in Fig. 12. For CB[8]/ZnO photocatalyst, the degradation rate was 99% in the first two recycles, but the degradation rate decreased significantly to 58% in the third recycle. The degradation rates of pure ZnO are all lower than those of CB[8]/ZnO at every recycle, revealing that the stability of CB[8]/ZnO is better than that of pure ZnO.

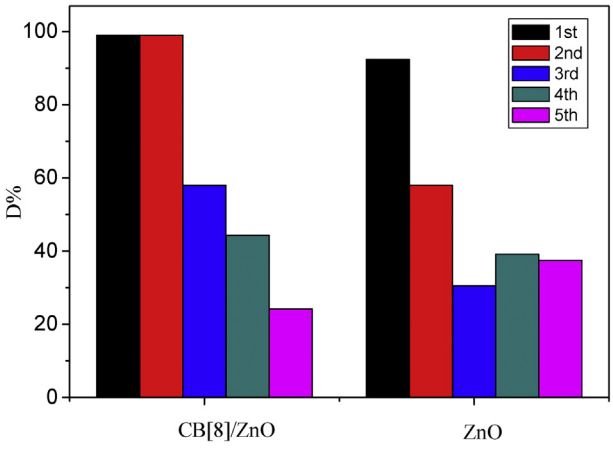

Fig. 12. Recycling efficiency of CB[8]/ZnO photocatalyst.

3.2.4. *Mechanism of photocatalytic activity*

Based on the above-mentioned results, we propose a possible mechanism to explain the charge transfer process and the degradation of organic dyes by CB[8]/ZnO composite under UV-visible light irradiation. The model is comprehensively illustrated in Scheme 2. On the interface of CB[8] and ZnO, Zn^{2+} ions chelate with the carbonyl groups of CB[8]. CB[8] has super-high adsorption capacity towards the adsorption of X-3B dye. In the dark reaction, the dye molecules were adsorbed on the surface of CB[8] or enter into the hydrophobic cavities of CB[8] to form an inclusion complex. Under UV-visible light irradiation, the photoexcitation of electrons (e^-) on the surface of ZnO takes place. Electrons from the valence band (VB) are transferred to the conduction band (CB) of ZnO, leaving holes (h^+) in the CB. The generated holes are attracted by the electron-rich carbonyl groups of CB[8], and are transferred to and trapped on the CB[8] units by means of Zn-O coordination bonds. The recombination of photoelectrons and holes is inhibited [30]. The holes trapped on CB[8] can oxidize those dye molecules that are on the surface or in the cavity of CB[8]. The electrons transferred to the CB can reduce O_2 dissolved in the solution to produce $\cdot O_2^-$, and the dye molecules in solution are oxidized by the $\cdot O_2^-$. CB[8]/ZnO composite could be activated effective by UV-vis light and exhibited an enhanced ability of photocatalysis towards the degradation of organic dyes. The probable reactions taking place during dye decolorization are summarized in Eqs. (1), (2), (3), (4), (5), and (6).

$$\text{CB[8]} + \text{dye} \rightarrow \text{CB[8]@dye} \quad (1)$$

$$\text{ZnO} + h\upsilon \rightarrow \text{ZnO}\ (e^- + h^+) \quad (2)$$

$$\text{CB[8]@dye} + h^+ \rightarrow \text{CB[8]@dye}\cdot(h^+) \quad (3)$$

$$\text{CB[8]@dye}\ (h^+) \rightarrow \text{oxidation of dye} + \text{CB[8]} \quad (4)$$

$$O_2 + e^- \rightarrow \cdot O_2^- \quad (5)$$

$$\cdot O_2^- + \text{dye} \rightarrow CO_2 + H_2O \text{ or degradation product} \quad (6)$$

To gain insight into the main roles of the distinct reactive species in UV-vis photocatalytic degradation, the X-3B solution was further reacted in the presence of different scavengers. In this work, triethanolamine (TEA), t-BuOH, benzoquinone (BQ), and CCl_4 were used as hole (h^+), hydroxyl free radical ($\cdot$OH), superoxide radical ($\cdot O_2^-$), and electron (e^-) scavengers [39]. An individual scavenger was added into the X-3B solution along with the CB[8]/ZnO photocatalyst prior to the UV-vis light illumination, and the degradation was monitored, as presented in Fig. 13. It can be found that the benzoquinone (BQ) and triethanolamine (TEA) immensely inhibit the degradation of X-3B dye, and the PCD efficiency was decreased from 89.4% to 3.7% and 16.1%, respectively. This indicates that $\cdot O_2^-$ and h^+ are primarily responsible for the photodegradation process under UV-vis light irradiation. To verify further the dominant role of $\cdot O_2^-$ in PCD degradation, N_2 was bubbled into X-3B solution for 30 min to drive away the O_2 dissolved in water, and the PCD efficiency was monitored. It is clear that N_2 bubbling has a strong inhibiting effect, and the PCD efficiency was decreased to 25.1%. t-BuOH and CCl_4 also inhibited the X-3B degradation to some extent, and the PCD efficiencies were decreased to 63.7% and 57.9%. This indicates that $\cdot$OH and e^- play a secondary role in the degradation of X-3B. Overall, the scavenger test results are in accordance with the proposed mechanism above. It is found that superoxide radicals and holes are the principle oxidative species that participate in photocatalytic reaction in the presence of CB[8]/ZnO photocatalyst.

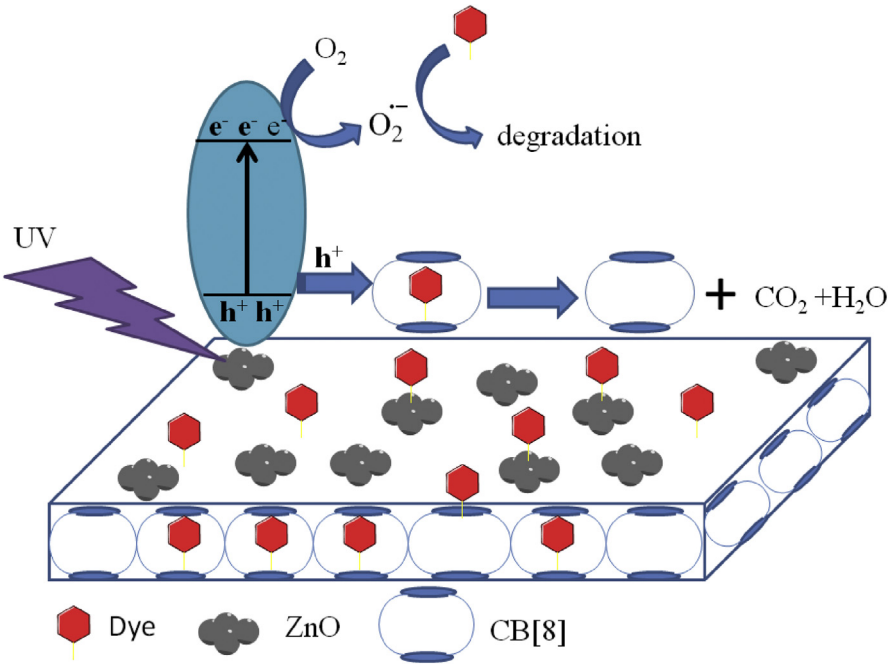

Scheme 2. Schematic illustration of the proposed photocatalytic mechanism of CB[8]/ZnO composite under UV-visible light irradiation.

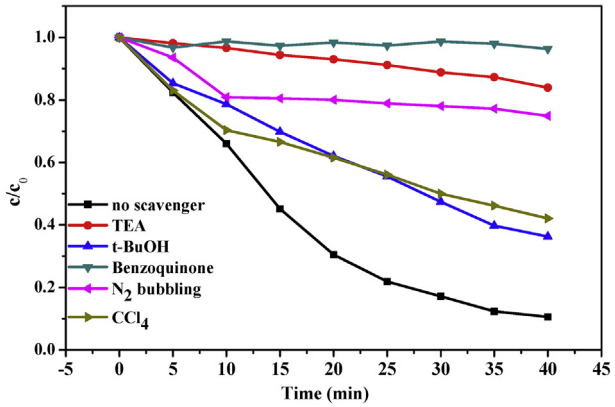

Fig. 13. The photocatalytic degradation of X-3B over CB[8]/ZnO photocatalyst in the presence of various scavengers.

4. Conclusion

Enhancing the separation of hole-electron pairs is one of the valid pathways to enhance the photocatalytic degradation performance of a semiconductor. In this work, cucurbit [8]uril/zinc oxide (CB[8]/ZnO) composite was synthesized, and the photocatalytic performance was estimated by the degradation of X-3B and X-RG dyes under UV-visible light irradiation. The photocatalytic degradation rate of CB[8]/ZnO composite was found to be six times that of pure ZnO. Zn^{2+} ions chelate with the carbonyl groups of CB[8] on the surface of CB[8]/ZnO. Under UV-visible light irradiation, the generated holes of ZnO are transferred to and trapped on the CB[8] units to facilitate the separation of electron-hole pairs, improving the photocatalytic performance of this system. The main reactive species that participate in the photocatalytic process are holes and superoxide radicals ($\cdot O_2^-$). The high PCD efficiency allows the use of CB[8]/ZnO composite as a potential photocatalyst for dealing with high concentrations of dye effluent.

Declarations

Author contribution statement

Lan Li, Lin Liu, Zhuang Li, Danling Hu: Performed the experiments; Analyzed and interpreted the data.

Chao Gao, Jinyan Xiong, Wei Li: Conceived and designed the experiments; Wrote the paper.

Funding statement

This work was supported by Foundation of Hubei Provincial Education Department (D20131605; 184043); Discipline Innovation Team Project of Wuhan Textile University (201401020).

Competing interest statement

The authors declare no conflict of interest.

Additional information

No additional information is available for this paper.

Acknowledgements

They also thank Dr. Tania Silver for critical reading of the manuscript.

References

[1] E. Forgacs, T. Cserhatia, G. Oros, Removal of synthetic dyes from wastewaters: a review, Environ. Int. 30 (2004) 953–971.
[2] P.S. Goh, A.F. Ismail, A review on inorganic membranes for desalination and wastewater treatment, Desalination 434 (2018) 60–80.
[3] E. Salehi, P. Daraei, A.A. Shamsabadi, A review on chitosan-based adsorptive membranes, Carbohydr. Polym. 152 (2016) 419–432.
[4] M. Khan, I.M.C. Lo, A holistic review of hydrogel applications in the adsorptive removal of aqueous pollutants: recent progress, challenges, and perspectives, Water Res. 106 (2016) 259–271.
[5] J.J. Murcia, M. Hernández-Laverde, H. Rojas, E. Muñoz, J.A. Navío, M.C. Hidalgo, Study of the effectiveness of the flocculation-photocatalysis in the treatment of wastewater coming from dairy industries, J. Photochem. Photobiol., A 358 (2018) 256–264.

[6] T. Robinson, G. McMullan, R. Marchant, P. Nigam, Remediation of dyes in textile effluent: a critical review on current treatment technologies with a proposed alternative, Bioresour. Technol. 77 (2001) 247–255.

[7] A. Kudo, Y. Miseki, Heterogeneous photocatalyst materials for water splitting, Chem. Soc. Rev. 28 (2009) 253–278.

[8] M. Sayed, A. Arooj, N.S. Shah, J.A. Khan, L.A. Shah, F. Rehman, H. Arandiyan, A.M. Khan, A.R. Khan, Narrowing the band gap of TiO_2 by co-doping with Mn^{2+} and Co^{2+} for efficient photocatalytic degradation of enoxacin and its additional peroxidase like activity: a mechanistic approach, J. Mol. Liq. 272 (2018) 403–412.

[9] M. Khodadadi, M.H. Ehrampoush, M.T. Ghaneian, A. Allahresani, A.H. Mahvi, Synthesis and characterizations of $FeNi_3$@SiO_2@TiO_2 nanocomposite and its application in photo-catalytic degradation of tetracycline in simulated wastewater, J. Mol. Liq. 255 (2018) 224–232.

[10] K.M. Lee, C.W. Lai, K.S. Ngai, J.C. Juan, Recent developments of zinc oxide based photocatalyst in water treatment technology: a review, Water Res. 88 (2016) 428–448.

[11] A.D. Mauro, M.E. Fragalà, V. Privitera, G. Impellizzeri, ZnO for application in photocatalysis: from thin films to nanostructures, Mater. Sci. Semicond. Process. 69 (2017) 44–51.

[12] S.M. Lam, J.C. Sin, A.Z. Abdullah, A.R. Mohamed, Degradation of wastewaters containing organic dyes photocatalysed by zinc oxide: a review, Desalin. Water Treat. 41 (2012) 131–169.

[13] C.B. Ong, L.Y. Ng, A.W. Mohammad, A review of ZnO nanoparticles as solar photocatalysts: synthesis, mechanisms and applications, Renew. Sustain. Energy Rev. 81 (2018) 536–551.

[14] C. Cao, L. Xiao, L. Liu, H. Zhu, C. Chen, L. Gao, Visible-light photocatalytic decolorization of reactive brilliant red X-3B on Cu_2O/crosslinked-chitosan nanocomposites prepared via one step process, Appl. Surf. Sci. 271 (2013) 105–112.

[15] C. Cao, L. Xiao, C. Chen, Q. Cao, Magnetically separable Cu_2O/chitosan-Fe_3O_4 nanocomposites: preparation, characterization and visible-light photocatalytic performance, Appl. Surf. Sci. 333 (2015) 110–118.

[16] D. Wu, X. Wang, H. Wang, F. Wang, D. Wang, Z. Gao, X. Wang, F. Xu, K. Jiang, Ultrasonic-assisted synthesis of two dimensional BiOCl/MoS_2 with tunable band gap and fast charge separation for enhanced photocatalytic performance under visible light, J. Colloid Interface Sci. 533 (2019) 539–547.

[17] K.K. Gangu, S. Maddila, S.B. Jonnalagadda, A review on novel composites of MWCNTs mediated semiconducting materials as photocatalysts in water treatment, Sci. Total Environ. 646 (2019) 1398–1412.

[18] K. Ravichandran, E. Sindhuja, Fabrication of cost effective g-C_3N_4+Ag activated ZnO photocatalyst in thin film form for enhanced visible light responsive dye degradation, Mater. Chem. Phys. 221 (2019) 203–215.

[19] S.M. Mousavi, A.R. Mahjoub, R. Abazari, Facile green fabrication of nanostructural Ni-doped ZnO hollow sphere as an advanced photocatalytic material for dye degradation, J. Mol. Liq. 242 (2017) 512–519.

[20] V.S. Kosera, T.M. Cruz, E.S. Chaves, E.R.L. Tiburtius, Triclosan degradation by heterogeneous photocatalysis using ZnO immobilized in biopolymer as catalyst, J. Photochem. Photobiol., A 344 (2017) 184–191.

[21] X. Zhou, X. Li, Y. Gao, L. Li, L. Huang, J. Ye, Preparation and characterization of 2D ZnO nanosheets/regenerated cellulose photocatalytic composite thin films by a two-step synthesis method, Mater. Lett. 234 (2019) 26–29.

[22] M. Chen, C. Bao, T. Cun, Q. Huang, One-pot synthesis of ZnO/oligoaniline nanocomposites with improved removal of organic dyes in water: effect of adsorption on photocatalytic degradation, Mater. Res. Bull. 95 (2017) 459–467.

[23] S. Karcher, A. Kornmuller, M. Jekel, Cucurbituril for water treatment. Part I: solubility of cucurbituril and sorption of reactive dyes, Water Res. 35 (2001) 3309–3316.

[24] X.M. Xie, X.L. Li, H.H. Luo, H.J. Lu, F.F. Chen, W. Li, The adsorption of reactive blue 19 dye onto cucurbit[8]uril and cucurbit[6]uril: an experimental and theoretical study, J. Phys. Chem. B 120 (2016) 4131–4142.

[25] X.L. Li, X.M. Xie, H.H. Luo, L. Li, Z. Li, Z.Y. Xue, W. Li, Adsorption of reactive yellow X-RG and reactive brilliant red X-3B onto cucurbit[8]uril and cucurbit[6]uril: effect factors, adsorption behavior and mechanism study, J. Colloid Interface Sci. 498 (2017) 31–46.

[26] H.H. Luo, X.Y. Huang, Y.H. Luo, Z. Li, L. Li, C. Gao, J.Y. Xiong, W. Li, Adsorption behavior and mechanism of acidic blue 25 dye onto cucurbit[8]uril: a spectral and DFT study, Spectrochim. Acta, Part A 193 (2018) 125–132.

[27] H.L. Cao, F.Y. Cai, H.B. Huang, B. Karadeniz, J. Lü, Polyoxometalate-cucurbituril molecular solid as photocatalyst for dye degradation under visible light, Inorg. Chem. Commun. 84 (2017) 164–167.

[28] J. Lu, J.X. Lin, X.L. Zhao, R. Cao, Photochromic hybrid materials of cucurbituril and polyoxometalates as photocatalysts under visible light, Chem. Commun. 48 (2012) 669–671.

[29] M. Cao, J. Lin, J. Lu, Y. You, T. Liu, R. Cao, Development of a polyoxometallate-based photocatalyst assembled with cucurbit[6]uril via hydrogen bonds for azo dyes degradation, J. Hazard Mater. 186 (2011) 948–951.

[30] Q. Yang, C. Fang, N. Zhao, Y. Jiang, B. Xu, S. Chai, Y. Zhou, Enhancing electron-hole utilization of CdS based on cucurbiturils vis electrostatic interaction in visible light, J. Solid State Chem. 270 (2019) 450–457.

[31] W.A. Freeman, W.L. Mock, N.Y. Shih, Cucurbituril, J. Am. Chem. Soc. 103 (1981) 7367–7368.

[32] J. Kim, I.S. Jung, S.Y. Kim, E. Lee, J.K. Kang, S. Sakamoto, K. Yamaguchi, K. Kim, New cucurbituril homologues: syntheses, isolation, characterization, and X-ray crystal structures of cucurbit[n]uril (n = 5, 7, and 8), J. Am. Chem. Soc. 122 (2000) 540–541.

[33] Z.F. Wu, S.J. Li, Infrared spectra characteristics of zinc hydroxide and zinc oxide, Chin. J. Spectrosc. Lab. 29 (2012) 2172–2175.

[34] V. Logvinenko, T. Mitkina, V. Drebushchak, V. Fedin, Thermal transformations of the supramolecular compound of cucurbit[8]uril with cobalt(III) complex {trans-$[Co(en)_2Cl_2]$@CB[8]}Cl·17 H_2O, J. Therm. Anal. 105 (2011) 103–106.

[35] M.J. Frisch, G.W. Trucks, H.B. Schlegel, G.E. Scuseria, M.A. Robb, J.R. Cheeseman, G. Scalmani, V. Barone, B. Mennucci, G.A. Petersson, H. Nakatsuji, M. Caricato, X. Li, H.P. Hratchian, A.F. Izmaylov, J. Bloino, G. Zheng, J.L. Sonnenberg, M. Hada, M. Ehara, K. Toyota, R. Fukuda, J. Hasegawa, M. Ishida, T. Nakajima, Y. Honda, O. Kitao, H. Nakai, T. Vreven, J.A. Montgomery Jr., J.E. Peralta, F. Ogliaro, M. Bearpark, J.J. Heyd, E. Brothers, K.N. Kudin, V.N. Staroverov, R. Kobayashi, J. Normand, K. Raghavachari, A. Rendell, J.C. Burant, S.S. Iyengar, J. Tomasi, M. Cossi, N. Rega, J.M. Millam, M. Klene, J.E. Knox, J.B. Cross, V. Bakken, C. Adamo, J. Jaramillo, R. Gomperts, R.E. Stratmann, O. Yazyev, A.J. Austin, R. Cammi, C. Pomelli, J.W. Ochterski, R.L. Martin, K. Morokuma, V.G. Zakrzewski, G.A. Voth, P. Salvador, J.J. Dannenberg, S. Dapprich, A.D. Daniels, O. Farkas, J.B. Foresman, J.V. Ortiz, J. Cioslowski, D.J. Fox, Gaussian 09, Revision D.01, Gaussian, Inc., Wallingford CT, 2009.

[36] N.M. O'Boyle, A.L. Tenderholt, K.M. Langner, Cclib: A Library for Package-Independent Computational Chemistry Algorithms, J. Comput. Chem. 29 (2008) 839–845.

[37] P. Germain, J.M. Letoffe, M.P. Merlin, H.J. Buschmann, Thermal behaviour of hydrated and anhydrous Cucurbituril: a DSC, T.G. and calorimetric study in the temperature range from 100 to 800 K, Thermochim, Acta 315 (1998) 87–92.

[38] X. Zhang, G. Li, Y. Wang, Microwave assisted photocatalytic degradation of high concentration azo dye Reactive Brilliant Red X-3B with microwave electrodeless lamp as light source, Dyes Pigments 74 (2007) 536–544.

[39] D. Vione, S. Khanra, S.C. Man, P.R. Maddigapu, R. Das, C. Arsene, R.I. Olariu, V. Maurino, C. Minero, Inhibition vs. enhancement of the nitrate-induced phototransformation of organic substrates by the ·OH scavengers bicarbonate and carbonate, Water Res. 43 (2009) 4718–4728.